1989LPSC...19...99H

Proceedings of the 19th Lunar and Planetary Science Conference, pp. 99-113
Copyright 1989, Lunar and Planetary Institute, Houston

The Lunar Swirls: Distribution and Possible Origins

L. L. Hood and C. R. Williams

Lunar and Planetary Laboratory, University of Arizona, Tucson, AZ 85721

Many of the strongest lunar magnetic anomalies correlate in location with swirl-like high- and low-albedo markings of the Reiner Gamma class. Models involving both meteoroid and cometary impact processes have previously been proposed to explain their origins. It has also been proposed that the high-albedo markings represent areas of the surface that have been magnetically shielded from the solar wind ion bombardment and have therefore not reached optical maturity. These models are investigated further here, using both correlative data analysis and theoretical modeling methods. Maps of the distribution of swirls on the lunar farside constructed from available orbital photography reveal relative concentrations in zones antipodal to Imbrian-aged basins where electron reflection maxima have previously been mapped. Correlative analyses show that electron reflection maxima are statistically correlated with both swirl locations and with the occurrence of probable seismically modified terrain produced at the times of the associated basin impacts. These results suggest that the relatively strong magnetization of basin antipode zones in some manner favored the formation of swirls in the same regions, i.e., the generation of swirls is not entirely exogenic. As a further test of the solar wind deflection model for swirl origins, trajectories of simulated solar wind ions deflected by the Lorentz force in the presence of model crustal magnetic fields are calculated numerically. For surface fields comparable in amplitude and horizontal scale with those measured at the Apollo landing sites ($B \leq 327$ nT), deflections are small and the net surface flux differs little from the incident solar wind flux. For surface fields with amplitudes and scales expected for the strongest observed orbital anomalies ($B > 1000$ nT), deflections are stronger and regions as large as 30 km in extent are partially shielded from the ion bombardment under nominal conditions. The shielded regions have curvilinear shapes and may be crossed by lanes with higher than average fluxes in a manner that depends on the details of the assumed surface field configuration. It is concluded that the solar wind deflection model provides a possible explanation for the unusual morphologies of these albedo markings and their preferred occurrence in basin antipode zones. Meteoroid impacts occurring in zones of strong preexisting crustal fields may also have contributed to the formation of the lunar swirls.

1. INTRODUCTION

Final mapping of the Apollo subsatellite magnetometer measurements showed that relatively strong orbital magnetic anomalies correlated with unusual swirl-like albedo markings including Reiner Gamma on western Oceanus Procellarum (Fig. 1) and with a second group of similar markings centered on the crater Gerasimovich on the farside (*Hood et al.*, 1979a; *Hood*, 1981). Swirls of the same type are found elsewhere on the eastern limb and farside; they generally show no relation to local topography and may represent only surficial alterations of the uppermost regolith (*Schultz*, 1976, pp. 420-423). Largely on the basis of comparisons with other lower-amplitude orbital anomaly sources, Reiner Gamma itself was suggested to represent an unusually magnetic deposit of secondary crater ejecta, perhaps produced by secondaries of the nearby Eratosthenian crater Cavalerius (*Hood et al.*, 1979b). This led to the original hypothesis of *Hood and Schubert* (1980) that preservation of a relatively high albedo for these regions and their unusual morphologies was due to deflection of the solar wind ion bombardment by the associated magnetic fields. This hypothesis is based on earlier experimental evidence that the presence of implanted solar wind hydrogen is a significant aid in the production of metallic phases in lunar agglutinate glasses (e.g., *Housley et al.*, 1973; *Housley*, 1977). Simultaneously, an alternate model for the formation of the swirls involving recent impacts of cometary comae onto the lunar surface was proposed (*Schultz and Srnka*, 1980a,b). In this model the swirls represent surficial scouring and/or residues of cometary comae impacts while the associated magnetic anomalies resulted from transient enhancements of the interplanetary magnetic field due to interaction of the cometary atmosphere with the Moon. For a discussion of other proposed origins for the swirls that predate the magnetics data, see *Schultz* (1976, pp. 420-423) and *El-Baz* (1972). *Bell and Hawke* (1981, 1987) have reported telescopic spectral observations that were interpreted as favorable for the cometary impact model for the origin of Reiner Gamma. These results have in turn led to further spectral studies of Reiner Gamma in search of water-bearing minerals for resource evaluation purposes. Although telescopic measurements by *Roush and Lucey* (1988) have ruled out the presence of abundant H_2O at Reiner Gamma, their measurements "do not exclude the presence of OH^--bearing minerals that have absorptions not detectable through the wet terrestrial atmosphere."

In this paper the origin of the lunar swirls is investigated further using both correlative data analysis and model calculations. In order for the secondary crater ejecta/solar wind deflection model to be valid, at least three conditions must be satisfied: (1) Strong lunar surface magnetic fields that are correlated with swirls must date from times $\ll 1$ b.y. ago to provide the required shielding of surface areas over geologic time; (2) magnetic fields at the lunar surface that are correlated with swirls must be sufficiently strong and coherent to markedly deflect incident solar wind ions; and (3) surface spectral properties must be significantly dependent on the ion bombardment, either directly via sputtering or indirectly via the catalytic presence of solar wind hydrogen. In order for the

© Lunar and Planetary Institute • Provided by the NASA Astrophysics Data System

1989LPSC...19...99H

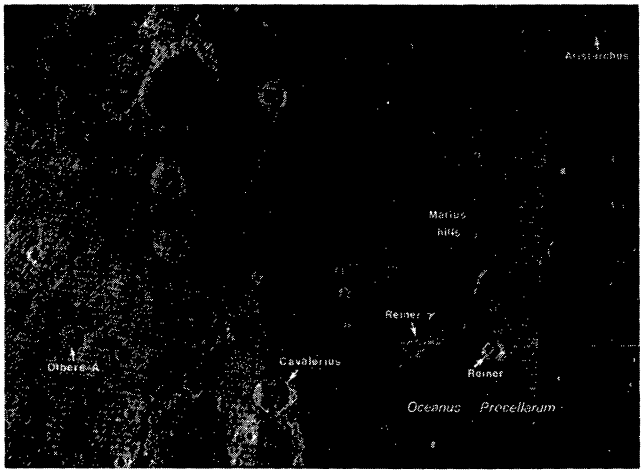

Fig. 1. Composite of Lunar Orbiter IV photographs showing Reiner Gamma and environs on western Oceanus Procellarum.

cometary impact model for swirl origins to be valid, swirls must be correlated with crustal magnetization that was imparted during relatively recent cometary impacts. Both the magnetization and the swirls should therefore be distributed in a manner consistent with the cometary impact process and should have no major relation to preexisting surface geology. In section 2 correlative studies are reported of the distribution of strong surface magnetic fields as measured by the electron reflection method versus major surface geology on the lunar farside. As reported previously by *Lin et al.* (1988; cf. *Hood,* 1981), the largest concentrations of surface fields detected by this method occur near the antipodes of the Orientale, Imbrium, Serenitatis, and Crisium basins. Swirl-like albedo markings similar in morphology to Reiner Gamma are present in or near the same zones. Strong surface fields in these regions are statistically associated with both swirl locations and unusual terrain interpreted to be the result of seismic modification occurring at the times of the basin-forming impacts. These results suggest that the strong crustal magnetic fields were produced at the time of formation of the basins (ca. 3.7-4.0 b.y. ago) in accordance with a proposed physical model (*Hood,* 1987). The tendency for swirls to occur in basin antipode zones rather than being randomly distributed on the farside indicates a possible relation to preexisting geology that is difficult to explain via purely exogenic models. In section 3 the question of whether lunar surface magnetic fields are capable of markedly deflecting incident solar wind ions is addressed. Numerical calculations are presented of the trajectories of simulated solar wind protons in model magnetic fields chosen to match as closely as possible those that are observed and inferred to be present at the lunar surface based on available Apollo measurements. Assuming that only the Lorentz force is important in the deflection process, it is found that surface fields greater than $\sim 10^{-3}$ nT with scales >10 km are required to produce strong deflections and accompanying surface flux reductions. Surface fields at sites of the strongest orbital anomalies are inferred to have amplitudes and scales of this order or larger. Complex surface fields produce curvilinear shapes for shielded regions as well as local zones with higher than average fluxes. Thus the second condition for validity of the solar wind deflection model may be satisfied. In section 4 the possible reconcilation of the solar wind deflection model for swirl origins with optical observations of the Moon, Mercury, and asteroids is examined. In section 5 a discussion emphasizing the need for future measurements is presented.

2. CORRELATIVE STUDIES

In agreement with earlier suggestions based on more limited data, the largest concentrations of strong surface fields detected by the electron reflection method have been found to occur at or near the antipodes of the four youngest large impact basins (*Lin et al.,* 1988). *El-Baz* (1971) first noted that the two largest concentrations of Reiner Gamma-type swirls on the farside occur near the Imbrium and Orientale antipodes. This was one factor that led some authors (e.g., *El-Baz,* 1972) to suggest that the swirls represent a recondensation or chemical alteration of the uppermost regolith by sublimates released from crustal fractures. Additional smaller swirl concentrations occur elsewhere on the farside, where strong magnetic anomalies were detected directly by the Apollo subsatellite magnetometers and indirectly by the limb compression method. One purpose of this section is to show that these concentrations occur near the antipodes of the Crisium and Serenitatis basins and correlate closely with the electron reflection maxima at the same locations (see also *Hood,* 1981).

A model for the formation of magnetic anomalies antipodal to basin-forming impacts has been developed in a semiquantitative form (*Hood,* 1987; see also *Hood and Vickery,* 1984). Briefly, a basin-forming impact occurring at an incident normal velocity greater than about 10 km s^{-1} will produce partial vaporization and ionization of silicate projectile and target material leading to the formation of a thermally expanding plasma cloud. Because the cloud is ionized and is characterized by a relatively high internal energy density, any ambient magnetic field (such as a solar wind magnetic field or a weak former lunar intrinsic field) will be excluded from the volume occupied by the impact plasma. As the cloud expands together with ballistically transported ejecta, lunar gravity will force the lower-energy components of the gas into trajectories that ultimately intersect at or above the basin antipode. Consequently, a compression of ambient plasma and magnetic field occurs in the antipodal zone leading to a magnetic field enhancement for a limited time interval [see Fig. 2 of *Hood* (1987)]. From conservation of magnetic flux and the scale sizes of magnetization concentrations in basin antipode zones (hundreds of kilometers), field amplifications by factors of several hundred may be estimated. Acquisition of remanent magnetization during the period of compressed field amplification may occur as a result of shock remanence by impact of solid secondaries from the basin impact or from compressive stresses generated by converging seismic waves.

In order to allow more detailed correlative studies of major surface geology, including swirl locations, with electron reflection measurements in the antipodal zones of the

© Lunar and Planetary Institute • Provided by the NASA Astrophysics Data System

1989LPSC...19...99H

Fig. 2. Portion of an Apollo 16 Hasselblad photograph showing Mare Marginis and swirl-like albedo markings of the Reiner Gamma class. For a full disk view including the same region, see frontispiece of the Apollo 16 Preliminary Science Report, *NASA SP-315,* 1972.

Orientale, Imbrium, Crisium, and Serenitatis basins, regional maps were constructed and reproduced in the top panels of Plates 1-3. Major geologic units shown were traced from the corresponding U.S. Geological Survey maps of *Wilhelms and El-Baz* (1977), *Stuart-Alexander* (1978), and *Scott et al.* (1977), respectively. These include young mare material (red), pre-Nectarian terra (brown), and furrowed and pitted material (blue) in Plates 1 and 2. *Schultz and Gault* (1975) have described photogeologic interpretations and model calculations strongly indicating that the latter unit is a result of convergence of seismic body and surface waves antipodal to the Orientale and Imbrium impacts. In Plate 3 several additional Orientale ejecta facies units (green and purple) were included. Although not shown on *Stuart-Alexander's* (1978) map, furrowed and pitted terrain is visible near the Serenitatis antipode (Lunar Orbiter I photograph 38M; see Fig. 4); a corresponding blue unit was therefore added to Plate 2. No furrowed and pitted material is visible near the Crisium antipode using the best available Zond 8 photography and may be masked by Orientale ejecta (cf. *Schultz and Gault,* 1975).

Maps of the distribution of lunar swirls on the eastern limb and farside as derived from available U.S. and Soviet orbital photography have previously been presented by *Schultz and Srnka* (1980a). In order to provide an independent evaluation, lunar images available in the Space Imagery Center at the Lunar and Planetary Laboratory were reexamined for the presence of Reiner Gamma-type swirls, i.e., higher and lower albedo markings with a curvilinear or sinuous shape. The locations of all clearly identified swirls are shown in the top panels of Plates 1-3 as dark markings superposed on the selenographic grid. Images examined included the Apollo 15, 16, and 17 metric camera photographs; selected Apollo 17 Hasselblad photographs; Lunar Orbiter I, II, III, IV, and V photographs; and Zond 8 photographs. As first pointed out by *Schultz and Srnka* (1980a), the albedo of swirls is a strong function of solar zenith angle and is especially enhanced at high solar phase angles [see Fig. 3 of *Shevchenko* (1984)]. Because orbital photographs with limited coverage were obtained at widely varying phase angles, the best measure of the overall number and lateral distribution of swirls across a large area is obtained from an examination of wide-angle photographs taken at a nearly constant (high) phase angle. (See, for example, the frontispiece of the Apollo 16 Preliminary Science Report, *NASA SP-315,* 1972.) Detailed studies of individual swirls are best carried out using high-resolution photographs obtained under variable solar illumination conditions. Selected frames containing swirls identifiable with minimum ambiguity (e.g., excluding curvilinear albedo markings coinciding with crater walls, etc.) are listed below separated according to the approximate region that they cover.

Mare Marginis region, eastern limb. Lunar Orbiter II, frames 75M, 196H, 196M; Lunar Orbiter III frames 121M, 121H; Lunar Orbiter IV frames 17H2, 18H, 157H1, 162H2, 192H; Lunar Orbiter V frames 181M, 163M; Apollo 16 frame AS16-3006; Apollo 17 Hasselblad frame AS17-150-23327. Numerous additional individual frames from Apollo 15, 16, and 17 metric cameras also exhibit bright swirls. However, these frames are limited in coverage and were obtained at variable phase angles so that it is difficult to compare the relative brightness and number of swirls on one frame to those on another. The same swirls are, however, visible on the wide-angle Apollo 17 Hasselblad (Fig. 2) and Apollo 16 metric camera frames listed above. We argue that the latter allow the best overall assessment of the relative brightness and distribution of swirls in this region. Coverage remains limited above about 20°N; this may result in some loss of information concerning the distribution of swirls to the north and northeast of Mare Marginis.

Mare Ingenii/Van de Graaff region. Lunar Orbiter II frame 75M and a Lunar Orbiter V frame show large numbers of swirls (Fig. 3). These are relatively large (as much as 40 km

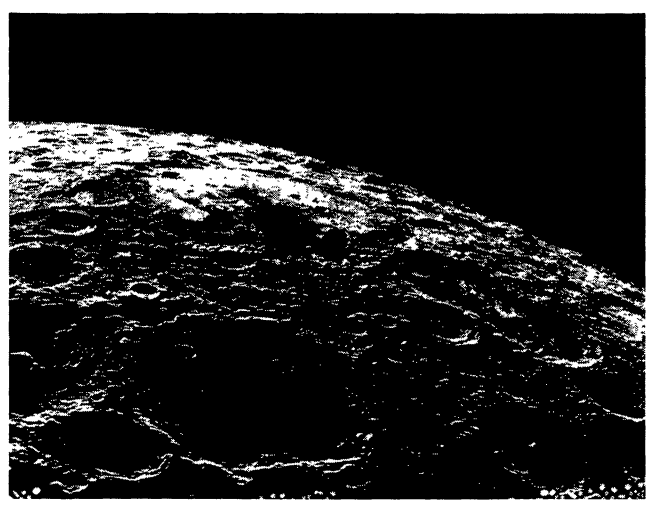

Fig. 3. Portion of a Lunar Orbiter V photograph including Mare Ingenii and nearby swirls. The double crater at right is Van de Graaff.

© Lunar and Planetary Institute • Provided by the NASA Astrophysics Data System

1989LPSC...19...99H

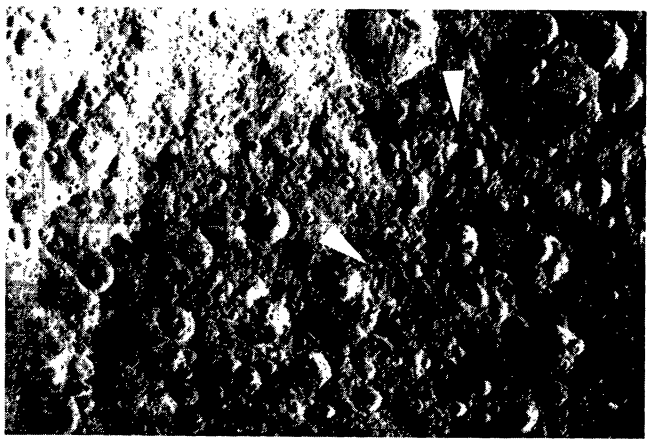

Fig. 4. Portion of Lunar Orbiter I frame 38M showing the region near the Serenitatis antipode (located at bottom center). This region is north of the Apollo basin; the 90-km crater Doppler is at top center. Small-scale swirl markings are visible at the lower left but are not prominent because of the unfavorable solar phase angle. Unusual terrain interpreted to be similar to that found antipodal to the Imbrium basin (e.g., lining the walls of Mare Ingenii) is indicated by the arrows.

in width) and distinct compared to swirls elsewhere on the farside.

Northwest of Apollo basin. Lunar Orbiter I frames 35M-40M, the most useful being frame 38M. The swirls in this region are relatively indistinct with lower albedo contrasts, although this is partly due to unfavorable solar phase angle (Fig. 4).

West of Orientale basin, centered on Gerasimovich. A Zond 8 photograph obtained at high solar phase angle (see *Hood,* 1981) shows a large group of bright swirls in this zone. The wide area covered by this photograph suggests that the clustering of swirls in this area is not a result of coverage bias.

A comparison of the resulting swirl maps on Plates 1-3 with those of *Schultz and Srnka* (1980a) shows general agreement, although there are some differences in detail. Most notably, there are fewer swirls east of Mare Marginis on the present maps than on the maps of Schultz and Srnka. We attribute this difference to the use of wide-angle photographs at nearly constant solar phase angle (i.e., excluding low-altitude Apollo metric and Hasselblad camera photographs) in order to better assess the relative brightness and number of individual swirls over a large region. As stated above, the primary photographs used to map swirls on Plate 1 were Apollo 16 frame AS16-3006 and Apollo 17 Hasselblad frame AS17-150-23327. Other swirls undoubtedly exist elsewhere on the farside, but they must occur in smaller groups and their identification is more ambiguous. From the present maps as well as those of Schultz and Srnka, it is evident that relative concentrations of swirls occur within the same basin antipode zones where strong surface magnetic fields were detected by the electron reflection method and other magnetic field mapping techniques (*Lin et al.,* 1988; *Hood,* 1981). In three of the four major farside zones, swirls occur in conjunction with nearby furrowed and pitted material that has earlier been attributed

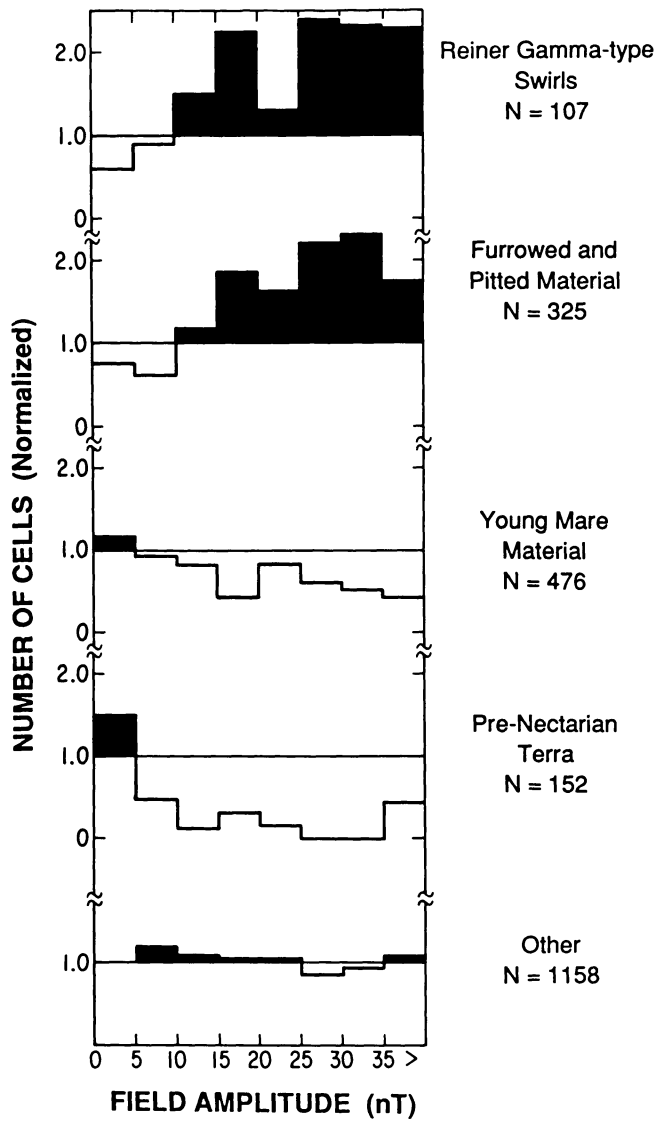

Fig. 5. Normalized occurrence rate for geologic units mapped in the top panel of Plate 1 plotted vs. the electron reflection field amplitude plotted in the lower panel of Plate 1. A value of unity on the ordinate scale represents a value equal to the average occurrence rate for all cells on the map. Values above unity are shaded for emphasis.

to antipodal seismic modification during the associated basin impacts (*Schultz and Gault,* 1975). As noted by the latter authors, the lack of similar terrain near the Crisium antipode may be due to obscuration by overlying Orientale ejecta.

Although electron reflection measurements of lunar crustal magnetic fields are not a substitute for direct magnetometer measurements at the lunar surface, it is well established that they provide the best remote measure of lateral variations in surface magnetic field strengths on the Moon (*Anderson et al.,* 1975; *Lin et al.,* 1988). Because the surface locations at which individual measurements are obtained depend upon the orientation of the interplanetary magnetic field as well as on

© Lunar and Planetary Institute • Provided by the NASA Astrophysics Data System

1989LPSC...19...99H

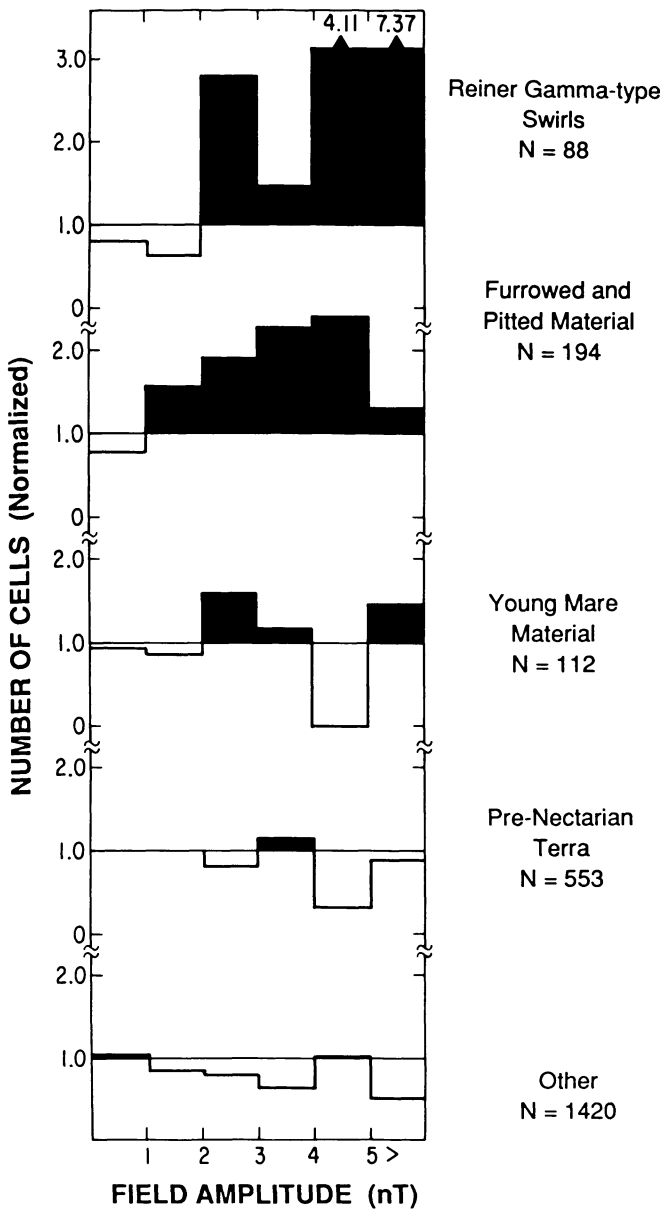

Fig. 6. Same as Fig. 5 but for geologic units and electron reflection measurements on both Plates 2 and 3.

the spacecraft location, the effective surface coverage of Apollo subsatellite electron reflection measurements is greater than that of the subsatellite magnetometers. In addition, the derived crustal field amplitudes are essentially independent of the subsatellite altitude, making them suitable for correlative studies with surface geology. However, it should be emphasized that the actual resolution and accuracy of the available electron reflection maps has not been fully demonstrated.

Electron reflection measurements are available in both a "high-resolution" (low electron energy) and a "low-resolution" (higher electron energy) form. The high-resolution measurements are limited to the lunar nearside and limb regions because a higher telemetry rate (requiring continuous spacecraft communication) was needed to transmit the data (for a color map, see the frontispiece of the *Proceedings of the Eighth Lunar Science Conference,* vol. 1, Plate 15, 1977). The low-resolution measurements possess complete longitude coverage but, like the high-resolution measurements, are limited to latitudes of less than about 35° (see Fig. 2 of *Lin et al.,* 1988). In this study a digital form of the high-resolution measurements mapped in 1.0° bins (provided by R. P. Lin) is used for correlative analysis of the Mare Marginis and east limb regions (lower panel of Plate 1) because of their increased coverage and apparent resolution within this zone. The low-resolution measurements are mapped in 1.25° bins and are used for analysis of the remaining regions (lower panels of Plates 2 and 3). To facilitate the correlative analysis, the top panel of Plate 1 was divided into 1.0° bins and occurrence data sets for each mapped geologic unit as well as the swirls were created in digital form. A similar procedure was applied to Plates 2 and 3 using a cell size of 1.25° to match the electron reflection measurements.

Figure 5 shows the normalized occurrence rate for each geologic unit in Plate 1 plotted vs. field amplitude at the effective measurement altitude in increments of 5 nT (1 nT = 10^{-5}G). The occurrence rates were calculated by dividing the number of cells of a given geologic unit within a given field increment by the total number of cells for that geologic unit on the map. These rates were then ratioed to the value obtained when all cells on the map are allowed rather than those of a single geologic unit. A normalized rate greater than (or less than) unity therefore indicates that the given geologic unit has a greater than (or less than) average number of cells within the given field increment. In the case of the Reiner Gamma swirls, any cell containing all or part of a bright swirl marking was assigned to the "swirls" unit in addition to the standard major geologic unit. Values above unity in Fig. 5 are shaded for emphasis. It is evident that cells containing Reiner Gamma-type swirls and cells containing furrowed and pitted material of probable seismic origin are each characterized by relatively high surface fields as compared to other units mapped in the top panel of Plate 1.

As an independent test of this result, the same procedure was applied to Plates 2 and 3 using the low-resolution electron reflection measurements available for these regions. The calculated normalized occurrence rates are plotted in Fig. 6. In this case the field amplitudes are smaller because the effective altitude that characterizes the low-resolution measurements is higher (compare the abscissa scales of Figs. 5 and 6). Again, both areas containing swirls and those containing visible furrowed and pitted material are characterized by larger than average occurrence rates of relatively high crustal fields. It should be emphasized that the results for the furrowed and pitted material are insensitive to our addition of such a unit near 160°W, 20°S in Plate 2. This added unit represents less than 10% of the total area for furrowed and pitted material (blue unit) on Plate 2. Remaining units on these maps are characterized by average or below-average occurrence rates of higher-amplitude fields.

© Lunar and Planetary Institute • Provided by the NASA Astrophysics Data System

1989LPSC...19...99H

From the results of Figs. 5 and 6, it may be inferred that high crustal fields in these basin antipode zones are statistically correlated with both swirl locations and with outcrops of probable seismically modified terrain formed at the times of the associated basin impacts. In the case of the swirls near the Crisium and Serenitatis antipodes, electron reflection maxima are closely correlated with the locations of swirl concentrations. As a result, the normalized occurrence rate for the "swirls" unit (top panel of Fig. 6) reaches very large values for the highest mapped field strengths. In the case of the Orientale and Imbrium antipode zones, broad electron reflection maxima cover large areas including both furrowed and pitted material and swirls. In these regions magnetic field maxima do not clearly coincide in all cases with swirl concentrations. Because the actual resolution of the electron reflection measurements has not been fully demonstrated, it is difficult to judge whether this lack of a direct correlation is real or is a measure of the accuracy of the field map in this region. In any case, there is a statistical correlation between electron reflection maxima and both swirls and seismically modified material as shown in Fig. 5.

A more accurate evaluation of the correlation between crustal field maxima and surface geology in these regions must await new orbital magnetometer measurements such as may be obtained by the planned Lunar Observer mission. At present, the only low-altitude direct magnetic field measurements over a lunar swirl marking were those obtained at altitudes of 20-30 km over Reiner Gamma (*Hood et al.,* 1979a,b). In this case the magnetic field maximum was closely correlated with the approximate center of the albedo marking. Forward model calculations showed that a near-surface magnetization source nearly coincident with the main albedo marking was consistent with the available measurements (*Hood,* 1980). [It is unlikely that the red halo surrounding the visible albedo marking (*Bell and Hawke,* 1981) is the anomaly source because a dip in the field amplitude near the center of the marking should have been observable at the relatively low subsatellite altitude.]

On the basis of these correlative results, particularly the occurrence of both magnetization concentrations and swirls in zones antipodal to four relatively young large basins, we suggest that many or all of the mapped crustal magnetic fields in these zones may date from the times of the Imbrian era basin impact events. In order for exogenic models including the cometary impact hypothesis to be valid, the occurrence of both the magnetization concentrations and the swirls in these zones must be regarded as fortuitous. The statistical correlation between electron reflection maxima and seismically modified terrain derived above would also be regarded as fortuitous. With currently available orbital magnetic field measurements, we cannot eliminate this possibility. However, the existing data do suggest that many or all of the magnetic fields that are correlated with swirl locations date from the times of the Orientale, Imbrium, Serenitatis, and Crisium impacts. If so, then it is worthwhile to consider in further detail models for swirl origins that depend on some property of preexisting geology. One proposed mechanism involves deflection of the solar wind ion bombardment by preexisting strong crustal magnetic fields. In the next section this mechanism is investigated further.

3. LUNAR SURFACE SOLAR WIND OBSERVATIONS AND INTERACTION MODELS

Direct solar wind spectrometer observations obtained at the Apollo 12 and 15 landing sites (*Clay et al.,* 1975) provide useful measurements of both the external plasma flow and perturbations of flow parameters caused by weak surface magnetic fields. At the Apollo 15 site the measured surface field was only 3 ± 3 nT, so the observed solar wind parameters were representative of the unperturbed plasma flow. At the Apollo 12 site the surface field was large enough (~38 nT) to produce small but measurable perturbations of incident plasma parameters. In particular, solar wind protons were observed to be decelerated by as much as 70 km/s and to be deflected in direction by $\leq 10°$. Unfortunately, no direct solar wind spectrometer data were obtained at other Apollo sites such as the Apollo 16 site, where surface fields as large as 327 nT were measured. Although the effects on the ion bombardment of the relatively small surface field at the Apollo 12 site were minor, it was recognized that stronger fields would induce progressively larger effects leading ultimately to a complete standoff of the ion bombardment. The authors therefore concluded that "those physical and chemical properties of the surface layers of the Moon which depend on the chemical composition, the energy, or the flux of the bombarding plasma may depend strongly on the strength of the local magnetic field." From the measurements of Clay et al., or from other measurements obtained in interplanetary space, the solar wind can be characterized as a plasma consisting dominantly of protons and electrons with a typical number density of each near 10 cm^{-3} and a typical flow velocity of 400 km s^{-1}, radially outward from the sun. In rare circumstances the bulk flow velocity may be as large as 1000 km s^{-1}, while the number density may be as small as ~2 cm^{-3}. For comparison, the thermal velocity of solar wind protons is much less than the flow velocity and averages about 50 km s^{-1} in the free solar wind.

The simplest model for the deflection of incident solar wind protons by a local magnetic field assumes that individual ions are subject only to the Lorentz force and that collective effects of the plasma interaction may be ignored. In reality the solar wind consists of both ions and electrons that are deflected in opposite directions by the magnetic field and that have very different gyroradii. The opposite deflections produce a current that amplifies the magnetic field by a factor as large as 2 at the plasma/field interface if a complete standoff of the incident plasma by the field is produced. The differing gyroradii allow protons to penetrate further into the magnetic field than the electrons, resulting in a polarization electric field in the boundary layer. The thickness of the boundary layer between the incident plasma and the confined magnetic field depends only on the plasma number density and is less than 2 km for typical solar wind conditions (*Hood and Schubert,* 1980). This charge-separation electric field effectively transfers momentum from the protons to the electrons and therefore decelerates

© Lunar and Planetary Institute • Provided by the NASA Astrophysics Data System

1989LPSC...19...99H

the protons. Both of these collective plasma effects will act to *increase* the deflections experienced by solar wind protons over those that would occur for single incident particles.

The problem of estimating the minimum dipole moment of lunar magnetic anomalies capable of strongly deflecting the solar wind ion bombardment was previously investigated analytically by *Hood and Schubert* (1980). Using an approximate model that accounted for boundary layer currents and electric fields, they estimated that the Reiner Gamma magnetic anomaly would shield a surface area of about 40 km in lateral extent for nominal solar wind conditions. This area is comparable to the actual area of the albedo marking. However, the distribution of surface ion fluxes for plausible surface field models was not investigated and the validity of the analytic approximations that were employed could not be absolutely verified. In this paper we take the alternate simpler approach of calculating numerically individual ion trajectories in realistic model magnetic fields to determine the corresponding flux at the lunar surface. Because this procedure neglects collective plasma effects and therefore underestimates slightly the deflection of the ions, it provides a "worst case" test of the ability of the strongest anomalies to shield surface areas from the solar wind. In addition, it allows the distribution of surface ion fluxes to be explicitly calculated for the assumed model assumptions to permit a qualitative comparison with the morphology of swirl albedo markings.

For simplicity, magnetic anomaly sources are represented by buried dipoles with moments m_i. This choice of a source model does not imply that lunar magnetic anomaly sources must consist of buried concentrated sources. A relatively thin magnetized surface layer, for example, is an equally plausible source model but is computationally inconvenient. The field above the lunar surface due to a uniformly magnetized disk is approximately the same as that of a dipole buried at a depth equal to the diameter of the surface disk. By employing a sufficiently large number of such dipoles, the source geometry and functional dependence of the magnetization on position can be simulated for an arbitrarily complex source body. A Cartesian coordinate system is defined with origin at the lunar surface; x is eastward, y is northward, and z is radial. Source dipoles are located at $((x_o(i),y_o(i),z_o(i))$ and are oriented relative to the x,y,z system by the angles (α_i,β_i). α_i is the tilt angle of the i-th dipole relative to z and β_i is the azimuth of the dipole tilt measured counterclockwise from the x direction. Defining x'_i,y'_i,z'_i as coordinates centered on the i-th dipole with z'_i parallel to the dipole moment vector, the magnetic field of the i-th dipole in this system is given by

$$B_{x'}(i) = \frac{m_i}{(r'_i)^5}(3x'_i z'_i)$$
$$B_{y'}(i) = \frac{m_i}{(r'_i)^5}(3y'_i z'_i) \qquad (1)$$
$$B_{z'}(i) = \frac{m_i}{(r'_i)^5}\,[3(z'_i)^2 - (r'_i)^2]$$

where $(r'_i)^2 = (x'_i)^2 + (y'_i)^2 + (z'_i)^2$. At any point x,y,z in the surface-centered system, the values of $B_{x'}(i)$, $B_{y'}(i)$, $B_{z'}(i)$ may be calculated using an appropriate coordinate transformation to relate x'_i,y'_i,z'_i to x,y,z. The net field components at x,y,z due to a total of N dipoles are

$$B_x = \sum_{i=1}^{N} [B_{x'}(i)\cos\alpha_i \cos\beta_i - B_{y'}(i)\sin\beta + B_{z'}(i)\sin\alpha_i \cos\beta_i]$$
$$B_y = \sum_{i=1}^{N} [B_{x'}(i)\cos\alpha_i \cos\beta_i + B_{y'}(i)\sin\beta_i + B_{z'}(i)\sin\alpha_i \sin\beta_i]$$
$$B_z = \sum_{i=1}^{N} [-B_{x'}(i)\sin\alpha_i + B_{z'}(i)\cos\alpha_i] \qquad (2)$$

Given that the magnetic field components at any point above the surface can be calculated from equation (2), the Lorentz acceleration components experienced by a charged particle with known velocity v_x,v_y,v_z are obtained from

$$\dot{v}_x = \frac{q}{m_p c}[v_y B_z - v_z B_y]$$
$$\dot{v}_y = \frac{q}{m_p c}[v_x B_x - v_x B_z] \qquad (3)$$
$$\dot{v}_z = \frac{q}{m_p c}[v_x B_y - v_y B_x]$$

where q is the particle charge, m_p is the particle mass, and c is the speed of light. Using equations (2) and (3) with a sufficiently small time step, the trajectory of a particle with known initial velocity and position can be calculated using a direct finite-difference method.

Model Calculations

Constraints on the distribution and orientation of remanent magnetic fields at the lunar surface are available indirectly from orbital measurements and directly from measurements at the Apollo 12 and 15 mare sites, at the Apollo 14 Fra Mauro site, and at the Apollo 16 Descartes highlands site (*Dyal et al.,* 1974). The measured fields at the two mare sites were relatively small: 38 ±2 nT at Apollo 12 and 3.4 ± 2.9 nT at Apollo 15 (1 nT = 10^{-5}G). On the other hand, fields measured at the Fra Mauro site were as large as 103 nT and those measured along a surface traverse at the Descartes highlands site were as large as 327 nT. These measurements are generally consistent with near-surface magnetization sources such as the Cayley formation (*Strangway et al.,* 1973). Apollo-era orbital magnetometer measurements were limited in coverage to narrow equatorial bands but nevertheless showed correlations of medium amplitude anomalies with basin ejecta materials including the Fra Mauro and Cayley formations (*Hood et al.,* 1979a,b). Both these observations and the surface magnetometer results are consistent with the generally larger ferromagnetic carrier content (metallic FeNi in the single domain size range) of highlands breccias and soils as compared to mare basalts (*Strangway et al.,* 1973). In rare cases orbital anomalies with amplitudes an order of magnitude larger (at a given altitude) than the Fra Mauro and Cayley anomalies were observed and were directly associated with Reiner Gamma-type swirls (*Hood et al.,* 1979a,b; *Hood,* 1981). By extrapolation from direct surface field measurements at the Apollo 16 highland site, surface field amplitudes at the sites of strong lunar anomaly sources are most probably of the order

© Lunar and Planetary Institute • Provided by the NASA Astrophysics Data System

1989LPSC...19...99H

TABLE 1. Isolated model dipole field parameters.

i	m_i, G-cm^3	$x_o(i)$, km	$y_o(i)$, km	$z_o(i)$, km	α_i	β_i
1	6.(15)	-60.	60.	-7.	90°	135°
2	4.(15)	0.	60.	-6.	90°	180°
3	6.(15)	60.	60.	-5.	90°	0°
4	6.(15)	-60.	0.	-7.	0°	0°
5	6.(15)	0.	0.	-7.	0°	180°
6	6.(15)	60.	0.	-10.	90°	90°
7	6.(15)	-60.	-60.	-7.	45°	45°
8	3.(15)	0.	-60.	-7.	90°	90°
9	1.5(15)	60.	-60.	-7.	90°	0°

Numbers in parentheses are powers of 10 by which primary entries are to be multiplied.

of or greater than 10^3 nT. This estimate is equivalent to the supposition that anomaly sources are near to the surface (no more than a few kilometers deep) rather than originating at large depths within the crust (*Strangway et al.,* 1973).

In order to investigate the dependence of calculated solar wind surface flux on the amplitude and orientation of a range of possible crustal magnetization sources, we consider first a series of isolated dipoles with differing magnetic moments, orientations, and depths of burial as listed in Table 1. Each dipole produces a field above the surface that is approximately equivalent to that of a uniformly magnetized surface disk with a diameter equal to the dipole depth and with a suitably chosen dipole moment per unit area. Thus the listed dipoles can be visualized as representing a distribution of near-surface magnetization as well as buried point sources. One important observational constraint that may be applied to these model magnetic fields is that their amplitude and scale must not be larger than that measured by the Apollo subsatellite magnetometers. Except for the Reiner Gamma anomaly (to be considered further below), the subsatellite magnetometer measurements were typically obtained at altitudes between 60 and 90 km above the surface. For example, magnetic field amplitudes at an altitude of 67 km above the Van de Graaff-Aitken region on the south-central farside were ~3.5 nT, while those above Gerasimovich on the east-central farside at an altitude of 88 km were ~2.0 nT (*Hood et al.,* 1981).

As shown in the top panel of Fig. 7, the field at a nominal subsatellite altitude of 67 km produced by the sum of the dipoles listed in Table 1 is less than 3.3 nT and is therefore consistent with that measured on the lunar farside by the Apollo subsatellites. The center panel of Fig. 7 shows the surface field amplitude for each of the nine listed dipoles. The surface maxima range from 400 nT for dipole number 9 to 4400 nT for dipole number 3. The bottom panel of Fig. 7

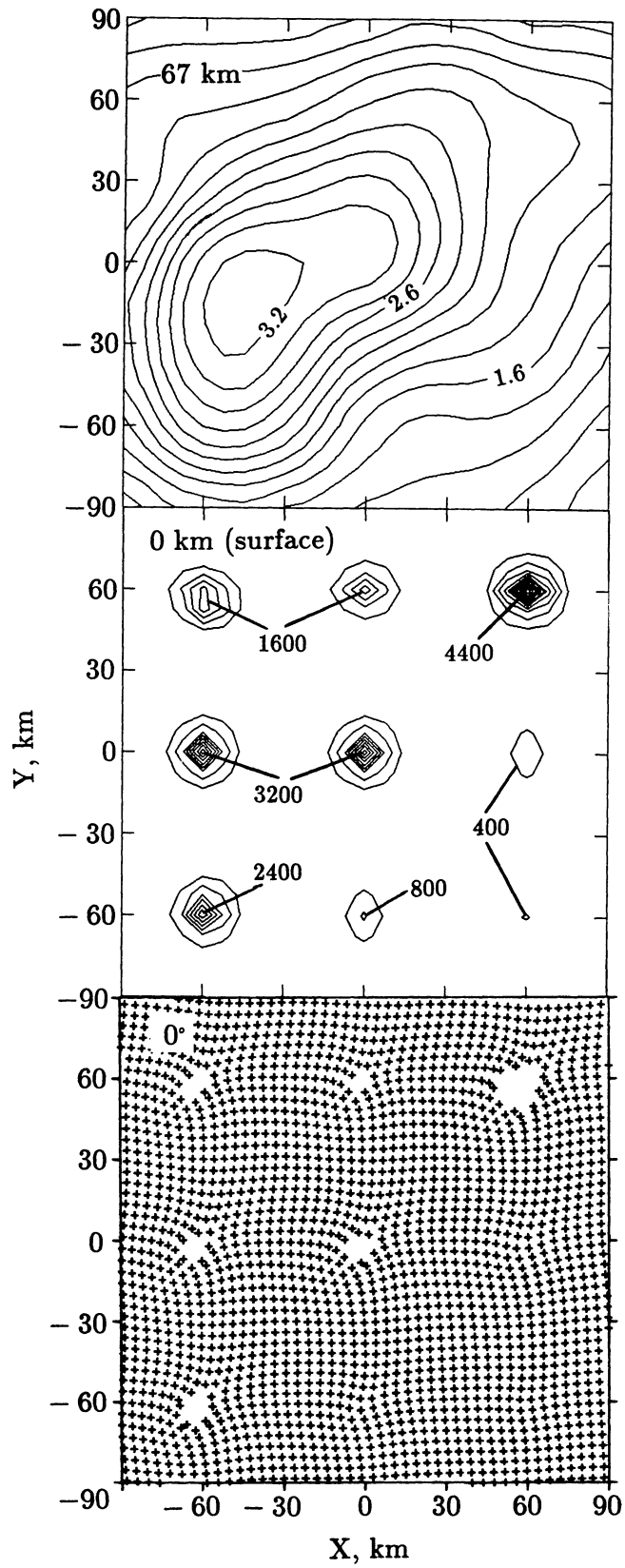

Fig. 7. The center panel shows the magnetic field amplitude (in nT) at the lunar surface due to nine model dipoles with parameters listed in Table 1. The top panel is the magnetic field amplitude at a nominal altitude of 67 km for comparison with measurements of crustal fields obtained by the Apollo subsatellites. The bottom panel plots the surface intersections of trajectories of simulated solar wind protons incident at an angle of 0° from the vertical onto the model magnetic field assuming that only the Lorentz force is important.

© Lunar and Planetary Institute • Provided by the NASA Astrophysics Data System

1989LPSC...19...99H

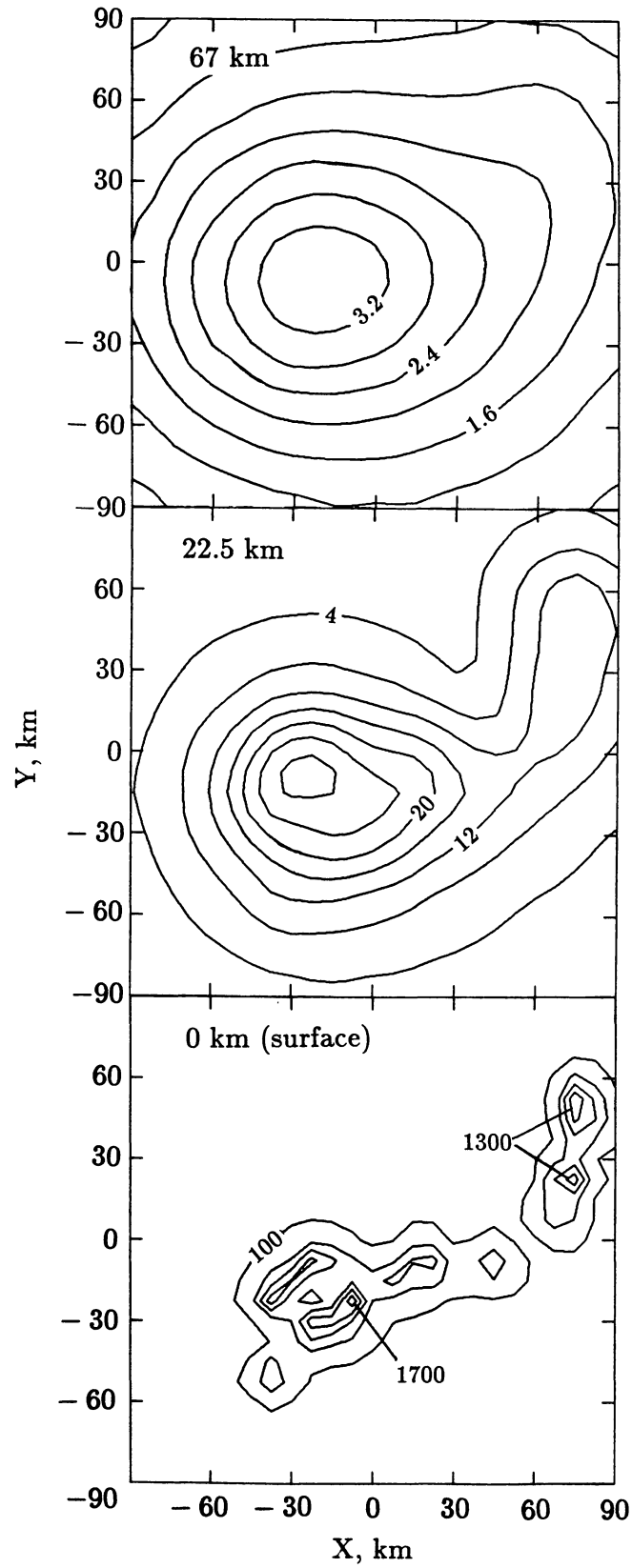

TABLE 2. Reiner Gamma model dipole parameters.

i	m_i, G-cm^3	$x_o(i)$, km	$y_o(i)$, km	$z_o(i)$, km	α_i	β_i
1	9.(14)	-36.	-22.5	-3.	63°	135°
2	9.(14)	-24.	-33.	-3.	63°	135°
3	7.7(14)	-36.	-51.	-3.	63°	135°
4	9.(14)	-12.	-31.5	-3.	63°	135°
5	1.(15)	-21.	-7.5	-3.	63°	135°
6	1.5(15)	6.	-15.	-4.	63°	135°
7	2.(15)	21.	-9.	-4.	63°	135°
8	8.(14)	-30.	-14.	-3.	63°	135°
9	1.1(15)	-10.	-10.	-3.	63°	135°
10	9.(14)	-7.	-24.	-3.	63°	135°
11	1.(15)	69.	9.	-3.	63°	135°
12	1.(15)	72.	24.	-3.	63°	135°
13	1.(15)	45.	-9.	-3.	63°	135°
14	1.(15)	78.	42.	-3.	63°	135°
15	1.(15)	78.	54.	-3.	63°	135°

shows the surface intersection points of the trajectories of simulated solar wind protons incident from the vertical (0°) with an initial velocity of 400 km/s. The protons were initially distributed in a rectangular array at an altitude of 500 km with a separation distance of 4 km. The deviation of intersection points (marked by "±" symbols) from this initial array at the surface indicates the extent of individual particle deflections by each model field. In the case of model fields with surface maxima less than ~800 nT, deflections are minimal and the resulting surface flux (indicated by the number of intersections per unit area) differs negligibly from the incident flux. As the amplitude increases above 1000-1200 nT, significant surface areas are shielded from the incident ions. Of course, the extent of incident ion deflections also depends on the horizontal scale of the magnetic anomaly field and on the orientation of the anomaly field. The scales considered here are representative of orbital anomalies detected at subsatellite altitudes (<100-150 km). In general, ions are deflected minimally if they are incident along the axis of the dipole moment vector and are maximally deflected if they are incident perpendicular to that axis.

In order to investigate further the deflection of incident ions in more realistic crustal fields, it is next of interest to consider an approximate model for the Reiner Gamma anomaly field. This anomaly was observed at lower altitudes (20-35 km) than any other strong crustal field detected with the subsatellite magnetometers. It possessed a maximum amplitude on one orbit pass exceeding 30 nT, although the final smoothed map amplitude is ~22 nT using all available orbits. From the modeling results of *Hood* (1980), a bulk direction of magnetization of $\alpha \approx 63°$ and $\beta \approx 135°$ was inferred although small-scale deviations from this direction of magnetization are allowed by the data. In order to produce a realistically complex surface field with an amplitude consistent with orbital measurements, 15 dipoles with this orientation located at depths of 3 to 4 km beneath the surface were selected as listed

Fig. 8. Reiner Gamma model magnetic field amplitude in nT at the indicated altitudes using the model parameters listed in Table 2.

© Lunar and Planetary Institute • Provided by the NASA Astrophysics Data System

1989LPSC...19...99H

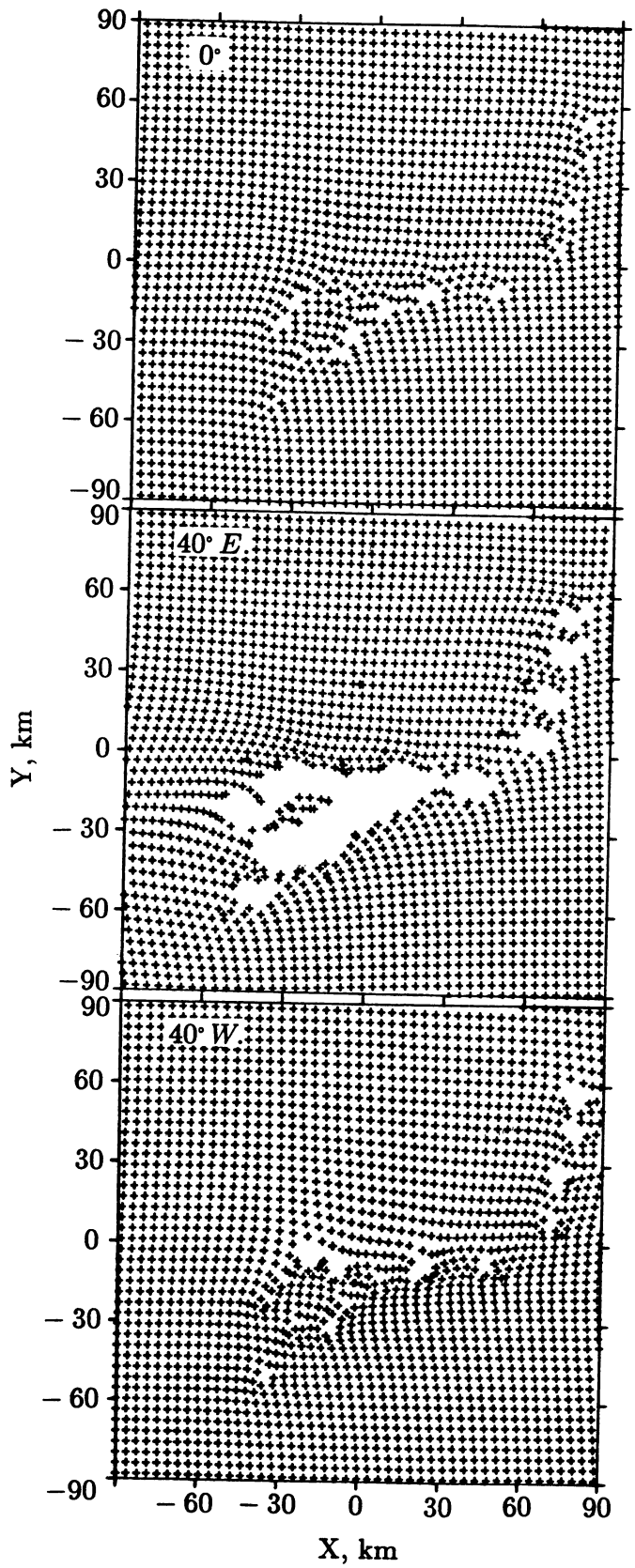

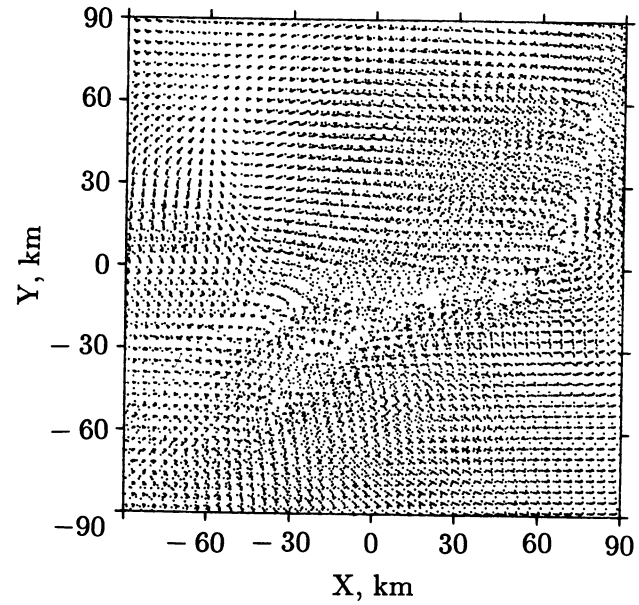

Fig. 10. Composite plot of surface intersections for simulated solar wind protons incident on the Reiner Gamma model magnetic field (Table 2). Seven different angles of incidence ranging from 60° west of the vertical to 60° east of the vertical are included. For clarity, individual intersections are plotted as dots rather than as crosses as in Fig. 9.

in Table 2. The surface locations of these dipoles were chosen to outline the shape of the visible albedo marking. Although this source model is not unique, it produces surface field amplitudes exceeding 1000 nT, as expected for strong anomaly sources, and has field amplitudes at subsatellite altitudes that are consistent with available measurements (Fig. 8). Shown in Fig. 9 are the surface patterns of deflected simulated solar wind protons incident at three different angles on this model magnetic field. Deflections are seen to be largest for eastward angles of incidence, since the resulting trajectories are nearly perpendicular to the model magnetic field. However, all angles of incidence produce some deflection. To simulate the integrated monthly cycle of solar wind ion fluxes, similar calculations were made for angles from the vertical of 0°, 20°E, 20°W, 40°E, 40°W, 60°E, and 60°W. The surface intersections for all of these angles of incidence are plotted as individual dots in Fig. 10. A net flux reduction remains evident with an outline approximating the albedo marking. In addition, flux excesses are present in local zones where the deflections by separate dipoles result in a net focusing of incident particles. It should be emphasized that the model field of Table 2 is undoubtedly still oversimplified in comparison to the actual field at the surface of Reiner Gamma. In particular, locally stronger fields may exist that would produce

Fig. 9. Surface intersections of simulated solar wind protons incident at the indicated angles onto the Reiner Gamma model magnetic field.

© Lunar and Planetary Institute • Provided by the NASA Astrophysics Data System

1989LPSC...19...99H

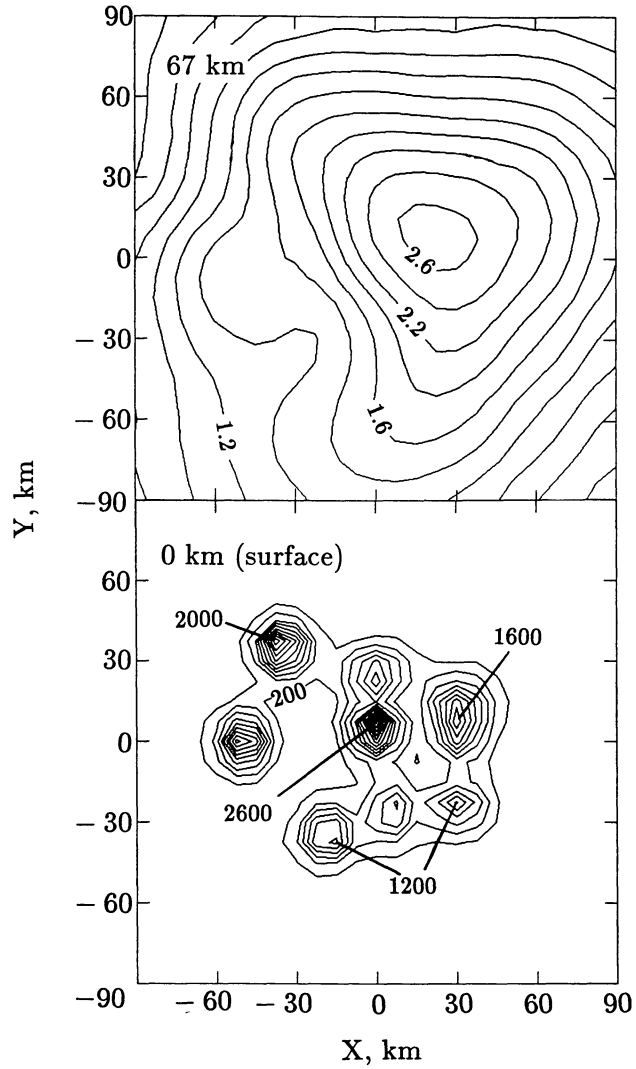

Fig. 11. Model magnetic field amplitudes in nT at the indicated altitudes for nine dipoles with parameters similar to those listed in Table 1 but with surface positions chosen to create a more realistic model field.

sharper edges between low and high flux zones. Alternately, sharper edges may be produced as a result of collective plasma flow effects not accounted for in these calculations.

As a second example of surface intersection patterns for a plausible model surface field, we consider nine dipoles with magnetic parameters similar to those of Table 1 but with epicentral locations that are chosen to produce a more complex field distribution. The resulting surface field amplitude map shown in the bottom panel of Fig. 11 exhibits a larger maximum amplitude of 2600 nT than the Reiner

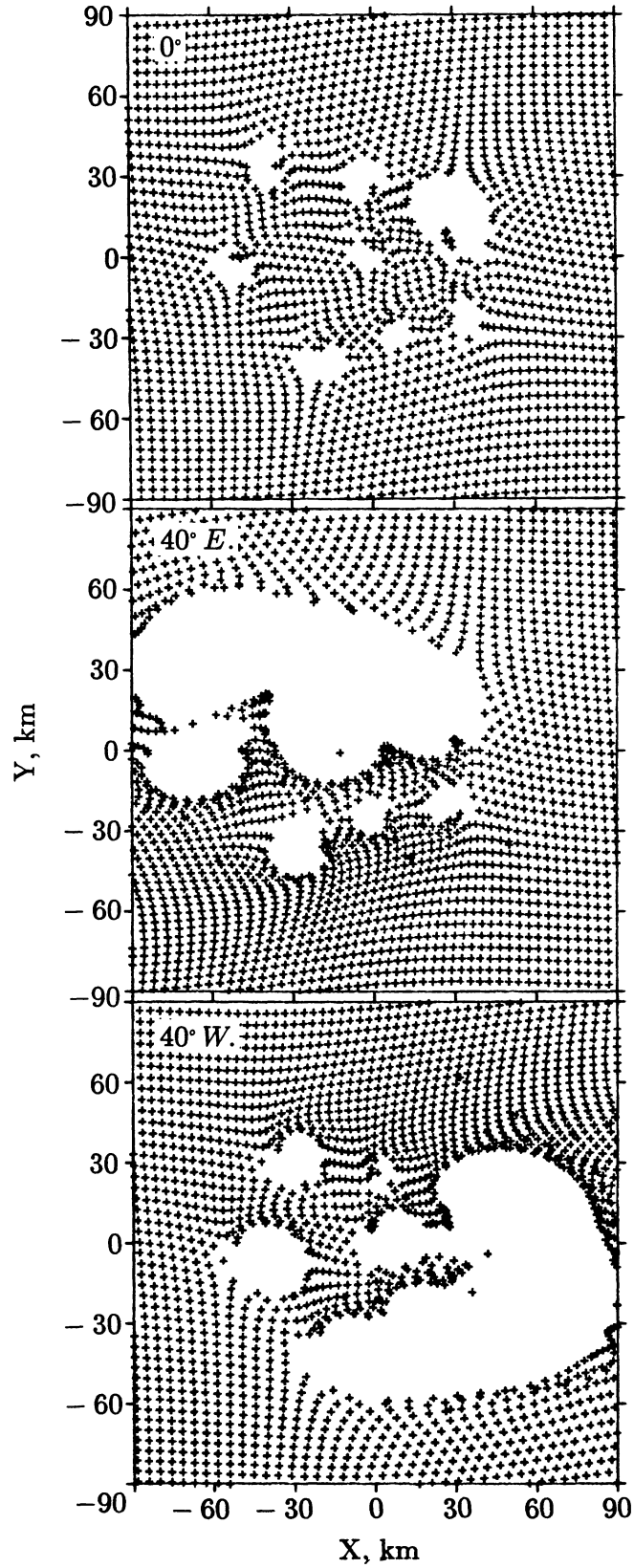

Fig. 12. Surface intersections of simulated solar wind protons incident at the indicated angles onto the model magnetic field of Fig. 11.

© Lunar and Planetary Institute • Provided by the NASA Astrophysics Data System

1989LPSC...19...99H

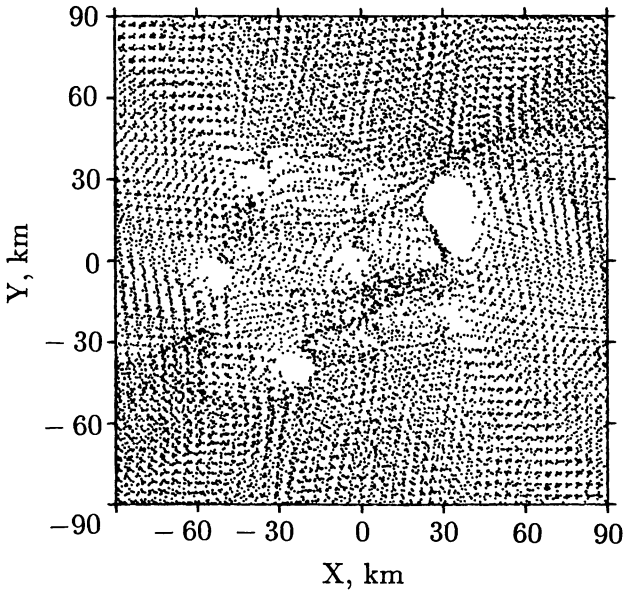

Fig. 13. Composite plot of surface intersections for simulated solar wind protons incident on the model magnetic field of Fig. 11. See the caption of Fig. 10 for further explanation. Note the presence of zones of higher surface flux as well as zones that are entirely shielded from the ion bombardment.

Gamma model field of Fig. 8. In addition, the directions of magnetization are more variable (compare Table 1 to Table 2). As shown in Fig. 12, the resulting surface intersection patterns are characterized by larger deflected zones that vary in shape for different angles of incidence. The integrated surface intersection pattern for angles between 60°E and 60°W is shown in Fig. 13. Because of the stronger surface fields, relatively sharp edges between high and low flux zones are produced, as well as concentrations of flux in some areas. Curvilinear shapes and "wispy" areas of flux reductions are also present.

4. MATURATION DARKENING MECHANISMS AND RELEVANT OPTICAL OBSERVATIONS

As stated in section 1, in order for the solar wind deflection model for swirl origins to be valid, it is necessary that surface optical properties be significantly dependent, either directly or indirectly, on the rate of surface ion implantation. In this section we briefly review relevant optical observations of the Moon and other exposed silicate bodies in the inner solar system to show that there is not a clear inconsistency between the solar wind deflection model and these observations.

Processes responsible for the generally low lunar visual albedo and for the darkening with time of freshly exposed surface materials such as crater rays have been investigated since the need to identify these processes was initially emphasized by *Gold* (1955). From this work it has become clear that the maturation darkening process involves the production during micrometeoroid impacts of agglutinate glasses containing either Fe and Ti metal, Fe and Ti oxides in dark minerals such as ilmenite, or both (e.g., *Wilhelms,* 1987, p. 94). The Fe and Ti content of mature regoliths depends at least in part on the composition of the parent materials with the result that the maria are darker than the highlands, and maria with higher contents of Fe and Ti are the darkest (*Adams and McCord,* 1970; *Pieters,* 1978). However, the dominant mechanisms by which Fe and Ti are concentrated in agglutinates have been difficult to identify experimentally. For a concise summary of proposed mechanisms for darkening lunar surface materials, see *Lin et al.* (1975).

Housley and others (*Housley et al.,* 1973; *Housley,* 1977; *Carter and McKay,* 1972) have described several mechanisms by which micrometeoroid impacts occurring in a regolith saturated in the uppermost layer with solar wind hydrogen can efficiently reduce silicates and provide an adequate source of Fe metal. These models are based in part on evidence that solar wind gases have provided the volatiles necessary for the generation of vesicles that are commonly present in lunar glasses and glass welded aggregates. *Hapke et al.* (1975) and *Wells and Hapke* (1977) have concluded that the concentration of Fe and Ti in agglutinates most probably occurs by redeposition on grain surfaces of material evaporated by either micrometeoroid impacts or by solar wind ion sputtering.

Moon/Mercury/Asteroid Comparisons

The disk-integrated visual albedo and reflectance spectrum of Mercury are very similar to that of the Moon (*Vilas and McCord,* 1976; *Veverka et al.,* 1988). This characteristic led *McCord and Adams* (1972) to suggest originally that Mercury must be covered with a soil rich in agglutinates as is the Moon. In a study of Mercury optical observations obtained by Mariner 10, *Hapke* (1977) argued that redeposition on grain surfaces of material vaporized in micrometeoroid impacts probably dominates over solar wind ion effects on both Mercury and the Moon, because Mercury shows no evidence for polar darkening relative to the equatorial zones. This argument rested on the observation that Mercury has a dipolar planetary magnetic field that was expected to allow solar wind or magnetospheric particles to impact the planet preferentially in the polar regions.

Although Mercury possesses an intrinsic global magnetic field, the field is relatively weak with surface amplitude ~170-350 nT, depending on the relative amplitudes of the dipole and higher-order moments (*Ness et al.,* 1975; *Whang,* 1977). In addition, the solar wind ion flux is nearly 7 times larger, on average, at Mercury's heliocentric distance than it is at 1 A.U. Consequently, this planetary-scale field is only just sufficient to keep the subsolar magnetopause boundary above the surface most or all of the time (*Goldstein et al.,* 1981). As reviewed in detail by *Russell et al.* (1988), the small size of Mercury's magnetosphere relative to the size of the planet and the absence of a significant atmosphere allow large fluxes of magnetospheric protons and heavier ions accelerated by substorm processes to impact the planetary surface at relatively low latitudes. There is little or no stable trapping region or plasmasphere, so that particles injected from the magnetotail

© Lunar and Planetary Institute • Provided by the NASA Astrophysics Data System

1989LPSC...19...99H

approximately consistent with lunar sample paleointensity data showing that relatively high fields existed in the lunar environment during the 3.6-3.9 b.y. interval (*Cisowski and Fuller,* 1986). A variety of other sample and orbital data indicate that most of the magnetization that is preserved in the lunar crust was acquired at times >3.0 b.y. ago. Consequently, we have been led to investigate causes other than relatively recent cometary impacts to explain the joint occurrence of strong magnetic anomalies and swirl-like albedo markings in these regions. In principle, the chemical alteration model of El-Baz and others (requiring postulated crustal fractures) could still be considered to explain the tendency for swirls to occur in basin antipode zones. However, the spectral data of *Bell and Hawke* (1981, 1987) provide no evidence for unusual compositional differences. Also, the chemical alteration model provides no definite explanation for the joint occurrence of swirls and magnetic anomalies. Thus we have investigated in more detail the solar wind deflection model, which predicts that swirls are areas whose spectral properties have been preserved or altered by the presence of the associated magnetic anomalies.

The numerical results of section 3 are consistent with, but do not prove, the solar wind deflection model for swirl origins. They indicate that surface fields at sites of strong magnetic anomalies must exceed $\sim 10^3$ nT on a scale of tens of kilometers to produce significant deflections. From a comparison with Apollo surface magnetometer measurements, it has been inferred that field amplitudes of this magnitude are most probably present at these sites. The numerical calculations have neglected several collective plasma effects that would tend to increase the deflection experienced by actual solar wind ions. It is therefore very probable that the strongest crustal field anomalies largely deflect and prevent the surface impingement of solar wind ions in the same zones where swirls are found. Thus this necessary condition for the viability of the solar wind deflection model appears to be satisfied. In section 4 we have summarized relevant optical measurements of exposed silicate surfaces in the inner solar system to show that these observations do not necessarily preclude the solar wind deflection model for lunar swirl origins. Indeed, one could conclude on the basis of these measurements that maturation processes involving *both* micrometeoroid impacts and solar wind ion implantation (e.g., *Housley et al.,* 1973) may be important.

On the other hand, it is clear from earlier work that solar wind ion deflection may not be the only process involved in the formation of the swirls. Several examples of ejecta "herringbone" patterns appear to be present in the Reiner Gamma main swirl and those south of it, suggesting the occurrence of one or more low-angle impacts (*Hood et al.,* 1979b). As proposed by these authors, the swirls may therefore represent secondary crater ejecta whose albedos have been selectively preserved by the associated magnetic anomalies. The resulting curvilinear patterns of ion deposition on these surfaces would then contribute to explaining their unusual morphologies. If the solar wind deflection model is ultimately disproved, then the correlative results of section 2 still strongly suggest that some property of basin antipode zones favors the formation of the swirls. For example, meteoroid impacts occurring in regions of strong crustal fields may deposit partially ionized ejecta or ejecta containing paramagnetic iron particles in swirl-like patterns because of magnetic forces on the ejected material. However, the solar wind deflection model has the virtue of simplicity and the numerical results of section 3 indicate that it is quantitatively feasible.

Finally, it must be admitted that Reiner Gamma is itself not antipodal to a young large impact basin. Although we have argued that relatively young basin-forming impacts probably dominated the production of strong magnetization that is preserved in the lunar crust, other smaller impacts or older basin impacts may have produced locally strong magnetization anomalies. The presence of such an anomaly on or beneath the surface of western Oceanus Procellarum has not been adequately explained by ourselves or by others. In that sense, even if the secondary crater ejecta/solar wind deflection model for the origin of the swirls is eventually verified, the origin of Reiner Gamma itself will continue to be an enigma.

In order to further resolve the issue of the origin of the lunar swirls, several classes of additional lunar measurements would be useful. Future Earth or lunar orbital spectral observations of Reiner Gamma, for example, may allow the detection or exclusion of small concentrations of residual water-bearing minerals with implications for the cometary impact model for swirl origins. Future higher-resolution lunar orbital magnetic field measurements may establish with greater certainty the correlation of locally strong magnetic fields with visible swirls. Solar wind spectrometer and magnetometer observations along a surface traverse at the site of a swirl marking such as Reiner Gamma will ultimately establish the existence or absence of any correlation between ion flux and albedo. In the interim, more precise numerical model calculations of the solar wind interaction with lunar crustal magnetic fields including collective plasma effects would be desirable. Finally, it should be emphasized that a combination of impact processes and solar wind ion deflection may be involved in the production of the lunar swirls. A complete geological and geophysical investigation of swirl sites may therefore be required to achieve a full understanding of their origins.

Acknowledgments. Discussions with B. R. Hawke, R. P. Lin, D. S. McKay, P. H. Schultz, and D. E. Wilhelms are appreciated. Some of these discussions helped to stimulate the ion trajectory calculations reported here. Critical written reviews by B. R. Hawke and P. H. Schultz of an earlier version of the manuscript were helpful. K. Denomy provided assistance in drafting Plates 1-3. A digital form of the Apollo subsatellite electron reflection measurements was supplied by R. P. Lin. Supported under NASA grant NSG-7020.

REFERENCES

Adams M. B. and McCord T. B. (1970) Remote sensing of lunar surface mineralogy: Implications from visible and near-infrared reflectivity of Apollo 11 samples. *Proc. Apollo 11 Lunar Sci. Conf.,* pp. 1937-1945.

Anderson K. A., Lin R. P., McGuire R. E., and McCoy J. E. (1975) Measurement of lunar and planetary magnetic fields by reflection of low energy electrons. *Space Sci. Instrum., 1,* 439-470.

© Lunar and Planetary Institute • Provided by the NASA Astrophysics Data System

1989LPSC...19...99H

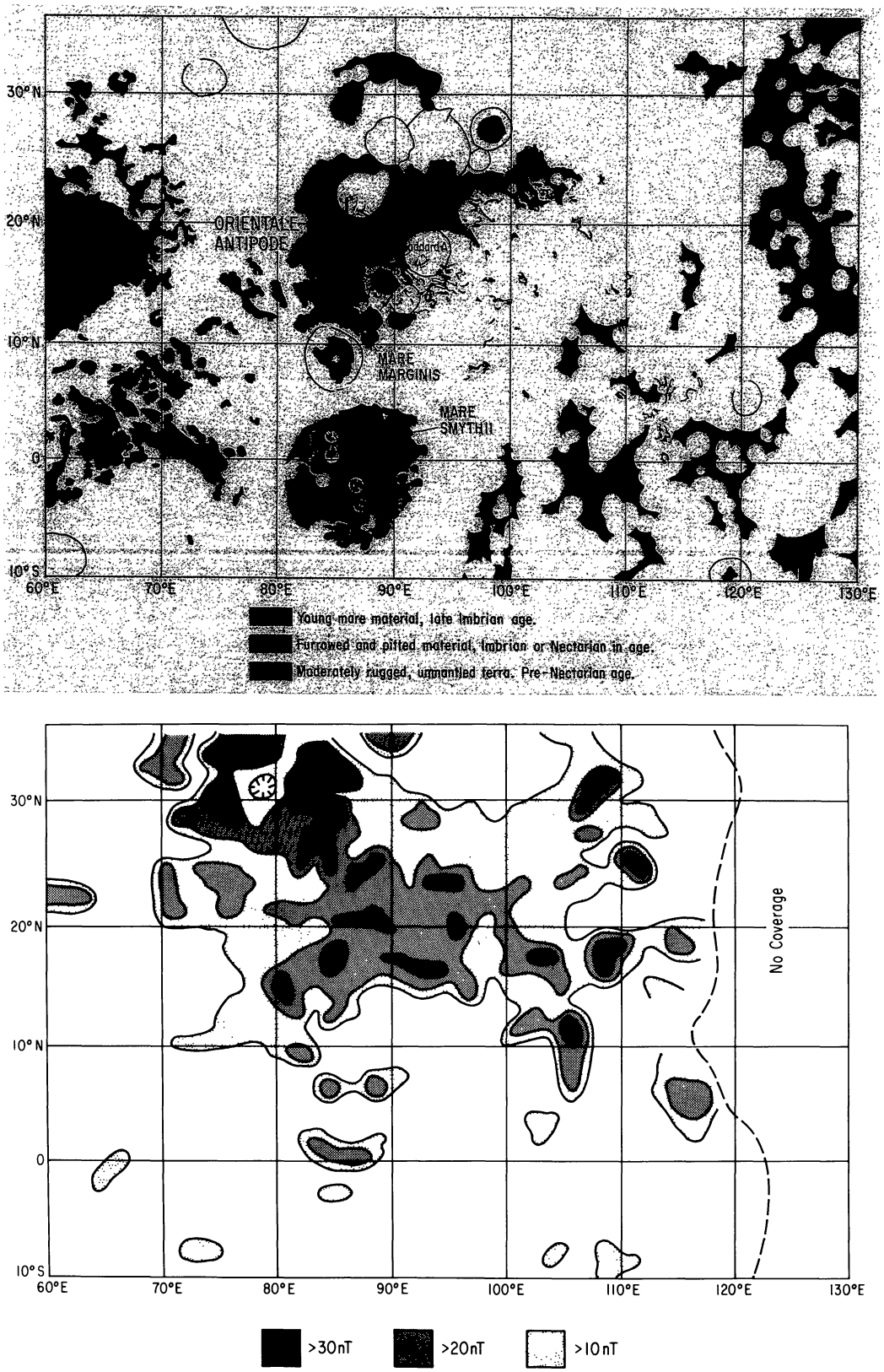

Plate 1. (Top panel) Approximate map of the distribution of swirl-like albedo markings visible on orbital photographs for a section of the eastern limb centered on Mare Marginis. Major geologic units are traced from *Wilhelms and El-Baz* (1977). The geometric location of the Orientale antipode is indicated. (Lower panel) Shaded contour map of electron reflection measurements across the same selenographic region covered by the top panel. See the text for a description of the electron reflection measurements.

© Lunar and Planetary Institute • Provided by the NASA Astrophysics Data System

1989LPSC...19...99H

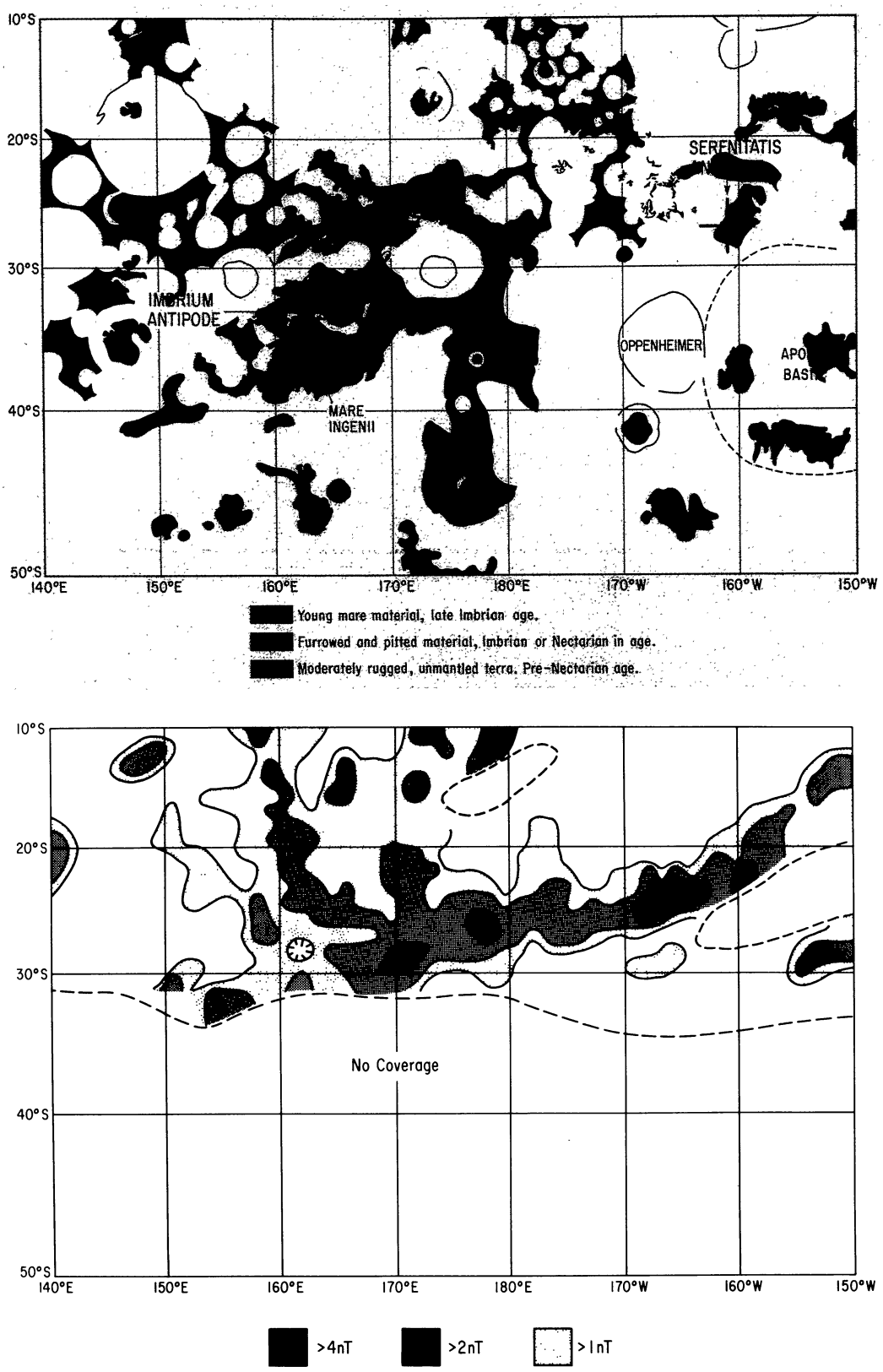

Plate 2. Same as Plate 1 but for a section of the south-central farside including the Imbrium and Serenitatis antipode zones. Major geologic units are traced from *Stuart-Alexander* (1978). Note that the measured electron reflection field amplitude is lower on the bottom panel and in Plate 3 than in Plate 1 because higher-energy electrons are employed (see text).

© Lunar and Planetary Institute • Provided by the NASA Astrophysics Data System

1989LPSC...19...99H

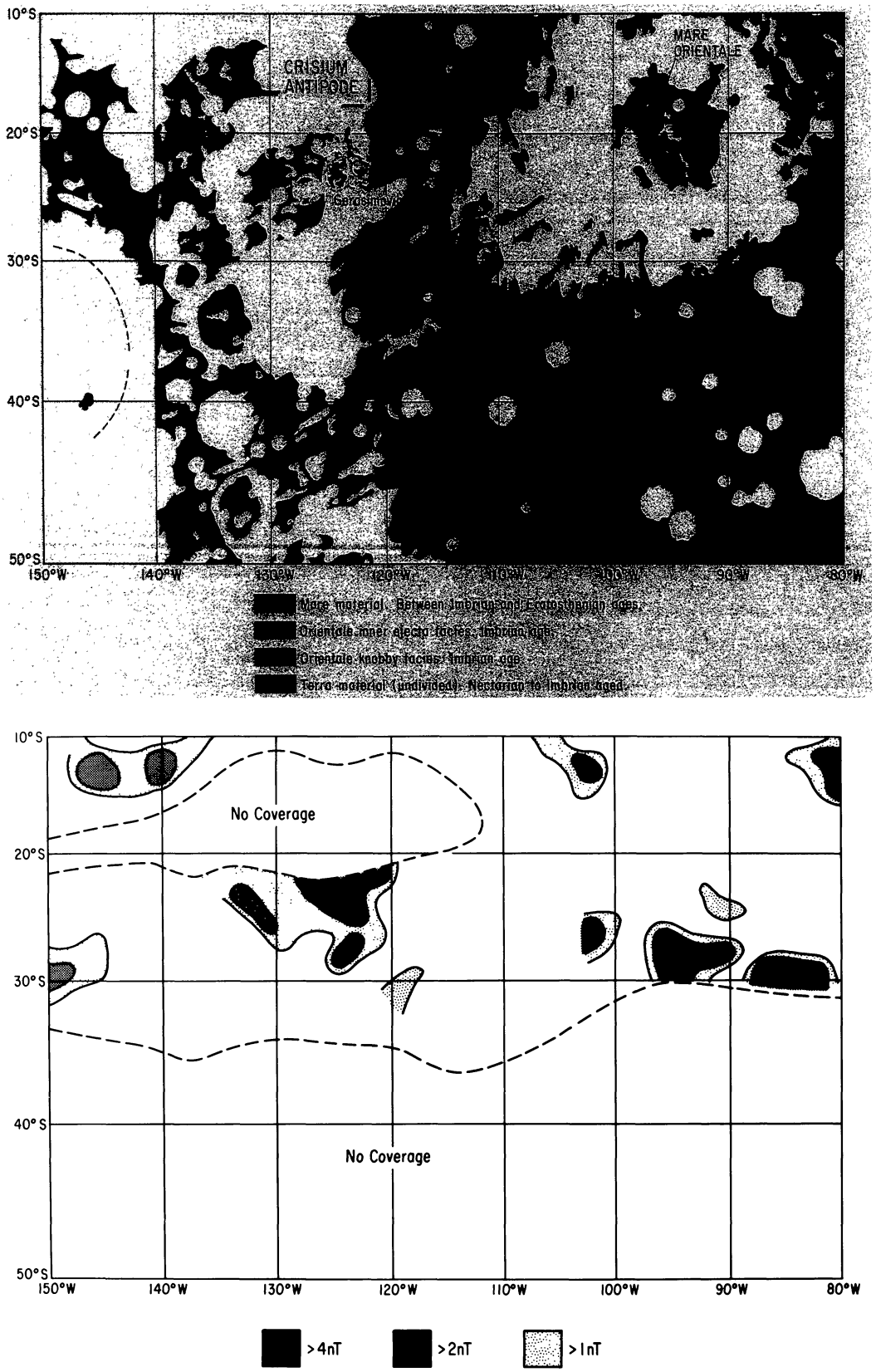

Plate 3. Same as Plate 2 but for a section of the southeastern farside including the Crisium antipode zone. Major geologic units are traced from *Scott et al.* (1977).

© Lunar and Planetary Institute • Provided by the NASA Astrophysics Data System

1989LPSC...19...99H

will directly impact the planetary surface. The preferred latitude range for particle precipitation is ~45°-70°, corresponding to a primary magnetic reconnection range of 3-6 planetary radii in the magnetotail (*Baker et al.,* 1986). However, some precipitation at higher latitudes resulting from direct entry of solar wind plasma into the polar cusps undoubtedly occurs; in addition, the geotail plasma sheet may extend almost to the planetary surface on the midnight side (Fig. 15 of *Russell et al.,* 1988), allowing significant precipitation at low latitudes as well. Thus, assuming that a sizable fraction (>1%) of solar wind protons obtain entry to the magnetosphere, these ions will ultimately be precipitated on the planetary surface at a rate that is not much less than occurs on the Moon. These ions will precipitate over a wide range of latitudes leading to an eventual saturation of the surface regolith with solar wind hydrogen. A strong pole/equator asymmetry of ion effects on surface optical properties is not necessarily expected. Therefore the original argument of *Hapke et al.* (1977) concerning the absence of a pole-to-equator albedo asymmetry for Mercury does not appear to be decisive.

Interestingly, from the above considerations, it may be suggested that only relatively strong crustal magnetic fields, if they exist on Mercury, would preclude ion precipitation on local areas of the surface. If locally strong crustal fields are present, then lunar-type swirl markings may be recognizable with improved photographic coverage of the surface. *Schultz and Srnka* (1980a) have in fact noted the probable occurrence of swirl-like albedo markings in two locations, but they caution that "it is impossible to verify this identification in detail." In any case, it seems premature to apply the existing Mercury optical and magnetic field observations to definitely exclude proton precipitation as a necessary element of the optical maturation process on both Mercury and the Moon.

Matson et al. (1977) have emphasized that asteroids, including large objects that presumably possess thick regoliths, are spectrally immature and some exhibit strong absorption bands indicative of fresh surfaces. A maturation process that depends solely on the solar wind ion bombardment would be expected to be operable in the asteroid belt since the solar wind flux there is still 0.1-0.4 times that at 1 A.U. (unless the process is strongly flux-dependent). Although this observation may imply that ion sputtering alone is not the primary maturation process, processes that depend on both the solar wind ion bombardment and on micrometeoroid impacts (e.g., *Housley et al.,* 1973) may not be excluded. *Matson et al.* (1977) have noted several differences in asteroid properties that would be expected to reduce the rate of micrometeoroid glass production and retention on asteroids relative to the Moon and Mercury (lower impact velocities, lower gravity, differences in regolith texture). Consequently, even if asteroid regoliths are saturated with solar wind hydrogen, these differences may be sufficient to retard the optical maturation process on asteroids relative to the Moon and Mercury. Hence these observations do not necessarily preclude the importance of solar wind ion implantation as a contributor to the optical maturation of the surfaces of the Moon and Mercury.

Lunar Spectral Observations

In an attempt to distinguish between the cometary impact and solar wind deflection models for the origin of the lunar swirls, *Bell and Hawke* (1981, 1987) analyzed telescopic near-infrared reflectance spectra for Reiner Gamma and vicinity. They found no evidence for exotic compositions and showed that the Reiner Gamma reflectance spectrum is closely matched by mixing models containing 90-95% fresh mare basalt and 5-10% highlands debris. They also noted the absence of dark halo craters (cf. *Wilhelms,* 1987) on the Reiner Gamma swirls, which they expected to be present if the swirls represented thin surficial layers of highlands anorthosite. Thus they showed that Reiner Gamma is not dominantly composed of highlands material but instead is composed mainly of mare material and may represent only an alteration or disruption of the preexisting mare regolith. They suggested that even if the absence of solar wind hydrogen has prevented microscopic iron generation and the consequent reddening of the continuum for the swirls, micrometeoroid glass production should still have suppressed the characteristic mare basalt pyroxene absorption bands. Since the latter are clearly observed, they concluded that the solar wind deflection model was unlikely and favored the cometary impact hypothesis.

Although *Bell and Hawke* (1981, 1987) have shown that Reiner Gamma is not composed dominantly of highlands material, it remains possible that this albedo marking represents an area of the mare surface that is dominantly shielded from the solar wind ion bombardment by locally strong magnetic fields. The secondary impactor model for the origin of the magnetic anomaly (including an association with Cavalerius) may therefore not be excluded if most of the ejected material was of mare composition. The only remaining objection that appears to preclude the solar wind deflection model concerns the suppression of the pyroxene absorption bands by micrometeoroid glass production (with or without generation of microscopic metallic Fe). A quantitative experimental test of this argument would be of interest. In some circumstances micrometeoroid impacts alone may ultimately darken a fresh lunar surface. However, the presence of solar wind hydrogen may be important for increasing the *rate* of optical maturation of lunar surface materials. Thus until a more definitive experimental test is performed, the possible contribution of solar wind ion deflection to the optical properties of Reiner Gamma may not be excluded.

5. DISCUSSION

In this paper we have attempted to investigate further several of the leading hypotheses for the formation of the lunar swirls. The correlative results of section 2 suggest that both swirls and strong concentrations of lunar magnetic anomalies ("magcons") tend to occur in zones antipodal to relatively young large impact basins. In our view, this joint occurrence of swirls and magcons at or near basin antipodes in close proximity to probable seismically modified terrain is unlikely to be fortuitous. The timing of these basin-forming events is

© Lunar and Planetary Institute • Provided by the NASA Astrophysics Data System

1989LPSC...19...99H

Baker D. N., Simpson J. A., and Eraker J. H. (1986) A model of impulsive acceleration and transport of energetic particles in Mercury's magnetosphere. *J. Geophys. Res., 91,* 8742-8748.

Bell J. F. and Hawke B. R. (1981) The Reiner Gamma Formation: Composition and origin as derived from remote sensing observations. *Proc. Lunar Planet. Sci. 12B,* pp. 679-694.

Bell J. F. and Hawke B. R. (1987) Recent comet impacts on the Moon: The evidence from remote-sensing studies. *Publ. Astron. Soc. Pac., 99,* 862-867.

Carter J. L. and McKay D. S. (1972) Metallic mounds produced by reduction of material of simulated lunar composition and implications on the origin of metallic mounds on lunar glasses. *Proc. Lunar Sci. Conf. 3rd,* pp. 953-970.

Cisowski S. M. and Fuller M. (1986) Lunar paleointensities via the IRMs normalization method and the early magnetic history of the Moon. In *Origin of the Moon* (W. K. Hartmann, R. J. Phillips, and G. J. Taylor, eds.), pp. 411-424. Lunar and Planetary Institute, Houston.

Clay D. R., Goldstein B. E., Neugebauer M., and Snyder C. W. (1975) Lunar surface solar wind observations at the Apollo 12 and Apollo 15 sites. *J. Geophys. Res., 80,* 1751-1760.

Dyal P., Parkin C. W., and Daily W. D. (1974) Magnetism and the interior of the Moon. *Rev. Geophys. Space Phys., 12,* 568-591.

El-Baz F. (1971) Light-colored swirls in the lunar maria. *Eos Trans. AGU, 52,* 856.

El-Baz F. (1972) The Alhazen to Abul Wafa swirl belt: An extensive field of light-colored, sinuous markings. In *Apollo 16 Preliminary Science Report,* pp. 29-93 to 29-96. NASA, Washington, DC.

Gold T. (1955) The lunar surface. *Mon. Not. R. Astron. Soc., 115,* 585-604.

Goldstein B. E., Suess S. T., and Walker R. J. (1981) Mercury: Magnetospheric processes and the atmospheric supply and loss rates. *J. Geophys. Res., 86,* 5485-5499.

Hapke B. (1977) Interpretations of optical observations of Mercury and the Moon. *Phys. Earth Planet. Int., 15,* 264-274.

Hapke B., Cassidy W., and Wells E. (1975) Effects of vapor-phase deposition processes on the optical, chemical, and magnetic properties of the lunar regolith. *The Moon, 13,* 339-353.

Hood L. L. (1980) Bulk magnetization properties of the Fra Mauro and Reiner Gamma formations. *Proc. Lunar Planet. Sci. Conf. 11th,* pp. 1879-1896.

Hood L. L. (1981) Sources of lunar magnetic anomalies and their bulk directions of magnetization: Additional evidence from Apollo orbital data. *Proc. Lunar Planet. Sci. 12B,* pp. 817-830.

Hood L. L. (1987) Magnetic field and remanent magnetization effects of basin-forming impacts on the Moon. *Geophys. Res. Lett., 14,* 844-847.

Hood L. L. and Schubert G. (1980) Lunar magnetic anomalies and surface optical properties. *Science, 208,* 49-51.

Hood L. L. and Vickery A. (1984) Magnetic field amplification and generation in hypervelocity meteoroid impacts with application to lunar paleomagnetism. *Proc. Lunar Planet. Sci. Conf. 15th,* in *J. Geophys. Res., 89,* C211-C223.

Hood L. L., Coleman P. J., Jr., and Wilhelms D. E. (1979a) The Moon: Sources of the crustal magnetic anomalies. *Science, 204,* 53-57.

Hood L. L., Coleman P. J., Jr., and Wilhelms D. E. (1979b) Lunar nearside magnetic anomalies. *Proc. Lunar Planet. Sci. Conf. 10th,* pp. 2235-2257.

Hood L. L., Russell C. T., and Coleman P. J., Jr. (1981) Contour maps of lunar remanent magnetic fields. *J. Geophys. Res., 86,* 1055-1069.

Housley R. M. (1977) Solar wind and micrometeorite effects in the lunar regolith. *Phil. Trans. R. Soc. London Ser. A, 285,* 363-370.

Housley R. M., Grant R. W., and Paton N. E. (1973) Origin and characteristics of excess Fe metal in lunar glass welded aggregates. *Proc. Lunar Sci. Conf. 4th,* pp. 2737-2749.

Lin L. I., Tsang T., and Adler I. (1975) Electron spectroscopic studies related to solar-wind darkening of the lunar surface. *Geophys. Res. Lett., 2,* 33-36.

Lin R. P., Anderson K. A., and Hood L. L. (1988) Lunar surface magnetic field concentrations antipodal to young large impact basins. *Icarus, 74,* 529-541.

Matson D. L., Johnson T. V., and Veeder G. J. (1977) Soil maturity and planetary regoliths: The Moon, Mercury, and the asteroids. *Proc. Lunar Sci. Conf. 8th,* pp. 1001-1012.

McCord T. and Adams J. (1972) Mercury: Surface composition from reflectance spectrum. *Science, 178,* 745-774.

Ness N. F., Behannon K. W., Lepping R. P., and Whang Y. C. (1975) The magnetic field of Mercury, 1. *J. Geophys. Res., 80,* 2708-2716.

Pieters C. M. (1978) Mare basalt types on the front side of the Moon: A summary of spectral reflectance data. *Proc. Lunar Planet. Sci. Conf. 9th,* pp. 2825-2849.

Roush T. L. and Lucey P. G. (1988) A search for water on the Moon at the Reiner Gamma formation, a possible site of cometary coma impact. *Proc. Lunar Planet. Sci. Conf. 18th,* pp. 397-402.

Russell C. T., Baker D. N., and Slavin J. A. (1988) The magnetosphere of Mercury. In *Mercury* (F. Vilas, C. R. Chapman, and M. S. Mathews, eds.), pp. 514-561. Univ. of Arizona, Tucson.

Schultz P. H. (1976) *Moon Morphology.* Univ. Texas, Austin.

Schultz P. H. and Gault D. E. (1975) Seismic effects from major basin formations on the Moon and Mercury. *The Moon, 12,* 159-177.

Schultz P. H. and Srnka L. J. (1980a) Cometary collisions on the Moon and Mercury. *Nature, 284,* 22-26.

Schultz P. H. and Srnka L. J. (1980b) Reply. *Nature, 287,* 86-87.

Scott D. H., McCauley J. F., and West M. N. (1977) Geologic map of the west side of the Moon. *U. S. Geol. Surv. Map I-1034.*

Shevchenko V. V. (1984) Optical properties of Reiner Gamma magnetic anomaly on the Moon (abstract). In *Lunar and Planetary Science XV,* pp. 772-773. Lunar and Planetary Institute, Houston.

Strangway D. W., Gose W., Pearce G., and McConnell R. K. (1973) Lunar magnetic anomalies and the Cayley formation. *Nature, 246,* 112-114.

Stuart-Alexander D. E. (1978) Geologic map of the central far side of the Moon. *U. S. Geol. Surv. Map I-1047.*

Veverka J., Helfenstein P., Hapke B., and Goguen J. D. (1988) Photometry and polarimetry of Mercury. In *Mercury* (F. Vilas, C. R. Chapman, and M. S. Mathews, eds.), pp. 37-58. Univ. of Arizona, Tucson.

Vilas F. and McCord T. (1976) Mercury: Spectral reflectance measurements (0.32-1.06 μm) 1974/75. *Icarus, 28,* 593-599.

Wells E. and Hapke B. (1977) Lunar soil: Iron and titanium bands in the glass fraction. *Science, 195,* 977-979.

Whang Y. C. (1977) Magnetospheric magnetic field of Mercury. *J. Geophys. Res., 82,* 1024-1030.

Wilhelms D. E. (1987) The geologic history of the Moon. *U. S. Geol. Surv. Prof. Paper 1348.* 302 pp.

Wilhelms D. and El-Baz F. (1977) Geologic map of the east side of the Moon. *U. S. Geol. Surv. Misc. Geol. Inv. Map I-948.*

© Lunar and Planetary Institute • Provided by the NASA Astrophysics Data System